Volume 1 | Number 1 | Jan 2013 | Pages 1–100

Journal of
Materials Chemistry C

Materials for optical and electronic devices
www.rsc.org/materialsC

ROYAL SOCIETY
OF CHEMISTRY

ROYAL SOCIETY
OF CHEMISTRY

www.rsc.org/materialsC

Journal Name

ARTICLE

Impact of molecular planarity on electronic devices in thienoisoindigo-based organic semiconductors

Takefumi Odajima[a] , Minoru Ashizawa[a,*] , Yuichi Konosu[a] , Hidetoshi Matsumoto[a], and Takehiko Mori[a,b]

Influence of molecular planarity on field-effect-transistor and photovoltaic-cell performance in thienoisoindigo derivatives has been studied. Thienoisoindigo derivatives end-capped with benzothiophene **TII(SB)$_2$** and benzofuran **TII(OB)$_2$** together with benzothiophene-capped isoindigo **II(SB)$_2$** are prepared, and their electronic properties are investigated. The crystal structures of **TII(SB)$_2$** and **TII(OB)$_2$** are determined by single-crystal X-ray structure analyses. The redox and optical measurements as well as the molecular orbital calculation indicate that thienoisoindigo-based molecules **TII(SB)$_2$** and **TII(OB)$_2$** have higher HOMO levels and smaller band gaps than **II(SB)$_2$**. The single-crystal structure analysis reveals that **TII(SB)$_2$** and **TII(OB)$_2$** have flat form, well agreeing with the structure optimized by the density functional theory (DFT) calculation, and **TII(SB)$_2$** and **TII(OB)$_2$** form slipped one-dimensional stacks with the alkyl chains extending out of the molecular plane. As an active layer of organic field-effect transistors, **TII(SB)$_2$** and **TII(OB)$_2$** show one order of magnitude larger p-type carrier mobility than that of **II(SB)$_2$**. It is noted that **TII(SB)$_2$** and **TII(OB)$_2$** fabricated on a tetratetracontane (TTC) modified substrate show balanced ambipolar properties ($\mu_h \approx \mu_e \approx 10^{-2}$ cm^{2}V^{-1}s^{-1}), where the carrier balance comes from well delocalized frontier molecular orbitals (FMOs). The photovoltaic properties of **TII(SB)$_2$**, **TII(OB)$_2$**, and **II(SB)$_2$** are investigated in bulkheterojunction devices using PC$_{71}$BM. The devices show a photovoltaic efficiency up to 2.4% for **TII(OB)$_2$** and 1.4% for **TII(SB)$_2$**. The device performance is closely associated with the flat structure of the thienoisoindigo unit, which effectively minimizes the steric interference of the benzothiphene and benzofuran units to facilitate the slipped co-facial π- π stacking.

Introduction

Organic semiconductors have gained much attention due to the applications to large area, flexible, and low-cost electronic devices, such as organic field effect transistors (OFETs), [1-4] light emitting diodes (OLEDs),[5,6] and photovoltaics (OPVs).[7-10] To date, tremendous research efforts have been devoted to develop high-performance small-molecule and polymer organic semiconductors, in which the field-effect mobility over 1 cm^2/Vs, and OPV devices with power conversion efficiency exceeding 9% have been attained.[11-14] In particular, materials showing ambipolar transport, where both electron and hole transports are possible, have been investigated extensively due to the application to OPV and ambipolar transistors.   As ambipolar organic semiconductors, polymers containing chemically bonded donor (D) and acceptor (A) units have advantages in realizing desirable donor and acceptor abilities by designing the D and A parts independently.   Representative electron accepting units are rylene diimide (naphthalene diimide and perylene diimide),[15,16] benzothiadiazole,[17] benzobisthiadiazole,[18,19] and diktopyrolopyrrole.[20-22]   The

excellent semiconducting properties of these molecules are associated with the widely extended frontier molecular orbitals (FMOs) with low-lying LUMO level, and molecular rigidity to form strong intermolecular packing. In addition, the alkyl chain substitution enhances the intermolecular interactions and the solubility in common organic solvents.

Recent D-A type polymers have shown excellent ambipolar properties because it is possible to achieve considerable intermolecular D-D and A-A interactions due to the segregated π-π stacking, In these D-A type polymers, the π-π stacking is expected from the X-ray diffraction, but in order to investigate the detailed molecular arrangement, we have to investigate the crystal structure of the monomer unit. However, ambipolar transistor performance of small molecules is still lower than those of polymers in general. Recently, ambipolar transistor properties have been reported in indigo derivatives.[23,24] Indigo is a dye produced from such plants as Indigofera tinctoria and Isatis tintora, which have been cultivated for at least four thousands of years for coloring textiles.[25] The structural isomer, isoindigo, has been also extensively studied as FET and OPV materials due to the easiness of the chemical modification.[26-29]
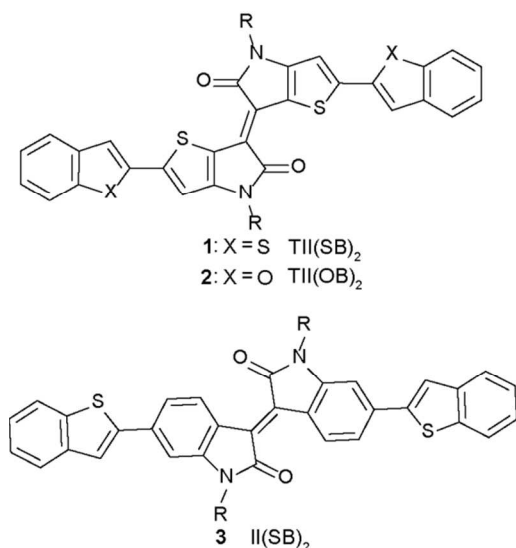
Scheme 1 Molecular structures of **1-3**.

Isoindigo is slightly twisted owing to the steric repulsion between the phenyl proton and the carbonyl oxygen. This twisted structure shortens the conjugation length and loosens the molecular packing. An attempt to remove this drawback is to replace the benzene ring with thiophene, in which the short oxygen-sulfur interaction of thienoisoindigo enhances the planarity. To date, a few thienoisoindigo copolymers with various electron-rich units have been reported as FET materials, where the hole mobilities are in the 10^{-1}-10^{-4} cm^{2}V^{-1}s^{-1} range.[30-32] A copolymer composed of thienoisoindigo and benzothiadiazole units has been reported to show balanced ambipolar charge transport with both types of carrier mobilities exceeding 0.1 cm^{2}V^{-1}s^{-1}.[33] In this context, it is interesting to explore the properties of thienoisoindigo-based small molecules

from the viewpoint of the influence of the molecular planarity on the device properties. This has prompted us to investigate thienoisoindigo-based small molecules end-capped with benzothiophene or benzofuran, in which planar thienoisoindigo component is expected to enhance the π-π intermolecular interaction for carrier transport. These end groups are previously combined with electron accepting groups such as thienyldiketopyrolopyrrole and pyridalthiazole groups, and the excellent OPV performance has been reported.[34-38]

Herein we report synthesis and properties of new small molecules **1** and **2**, where a thienoisoindigo unit is capped with benzothiophene or benzofuran (Scheme 1). These molecules are regarded as a minimal unit of the D-A type polymers, and we can investigate the molecular structures by using the crystal structure analysis. We also investigate the isoindigo analogue **3** in order to examine the effect of molecular planarity on the OFET and OPV properties (Scheme 1). Alkyl chains are introduced to enhance the solubility in organic solvents for facilitating the solution-process device fabrication. OFET and OPV properties of **1-3** are discussed in view of electronic structure, thin film morphology, and charge transport property.

Results and Discussion

Molecular Orbital Calculation

To examine electronic structures of **1-3**, density functional theory (DFT) calculations using Gaussian 09 program based on the B3LYP/6-31G*(d,p) level have been performed.[39] For simplifying the calculation, the alkyl groups are replaced with methyl groups. Figure 1 shows optimized molecular structures and the calculated HOMO and LUMO orbitals of **1-3**. The optimized molecular geometries of **1** and **2**
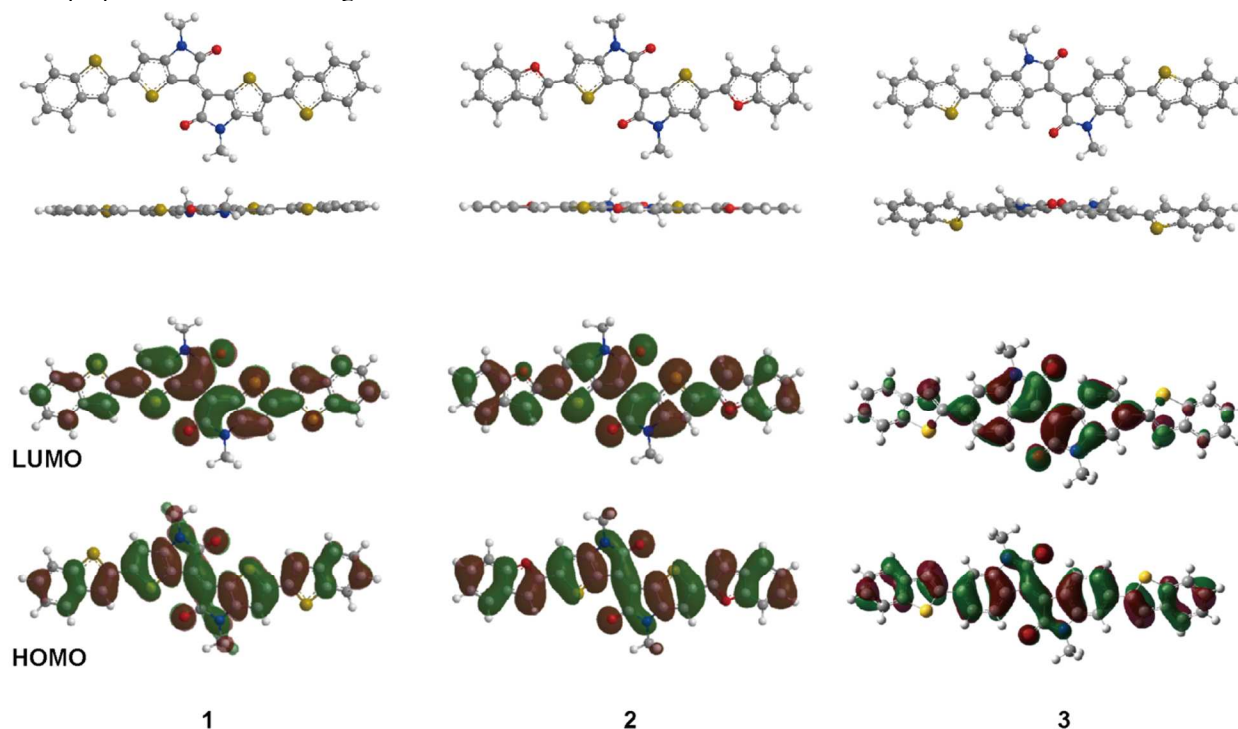
Fig. 1 Optimized molecular geometries and the calculated distributions of HOMO and LUMO of **1-3** obtained from the DFT calculations.
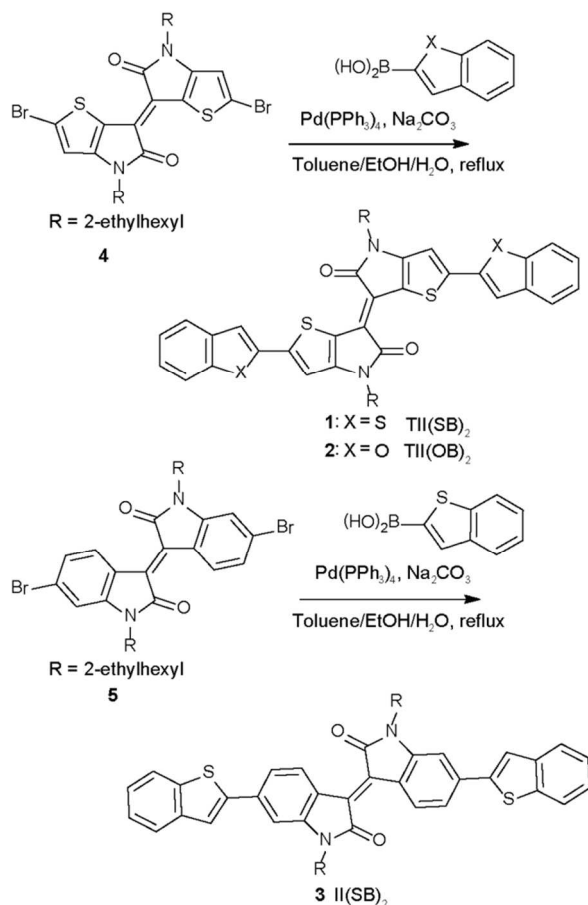
Scheme 2 Synthesis of **1-3**.

are almost flat, while **3** is non-planar; the benzothiphene ring is twisted from the isoindigo (II) unit with the dihedral angles of 23.9°, and the II plane is bent by 11.3°. The calculated HOMO and LUMO levels are -5.05 eV and -3.13 eV for **1**, -5.04 eV and -3.13 eV for **2**, and -5.36 eV and -2.87 eV for **3**, respectively. The HOMO and LUMO of **1** and **2** are delocalized over the π-conjugated skeletons, whereas, especially, the LUMO of **3** is mainly concentrated on the central II moiety. These calculations demonstrate how the π-conjugation lengths of **1** and **2** increase due to the molecular planarity. As a result, the HOMO-LUMO gaps of **1** and **2** (1.91~1.92 eV) are smaller than that of **3** (2.49 eV).

Synthesis and Thermal properties

Synthesis of **1-3** is outlined in Scheme 2. The brominated compounds **4** and **5** were prepared according to the previous reports.[33, 40] In order to improve the solubility and film forming ability, branched 2-ethylhexyl groups were introduced. The molecules **1-3** were prepared through the Suzuki-Miyaura coupling of **4** and **5** with benzothiophene and benzofuran boronic acid using Pd(PPh$_3$)$_4$ catalyst in toluene-ethanol.[41] The obtained **1-3** were soluble in common organic solvents. Chemical structures and purity were fully characterized by ^{1}H-NMR, mass spectroscopy, and elemental analysis. Thermal properties have been investigated by thermogravimetric analysis (TGA) and differential scanning calorimetry (DSC) analysis (Fig. S1). In these molecules **1-3**, the decomposition temperatures defined at 5% weight loss in TGA are higher than 350 °C due to the high thermal stability. The melting

points determined by the onset of the endothermic peaks in the heating runs of DSC are 290 °C for **1**, 292 °C for **2**, and 250 °C for **3**. The higher crystallization temperatures are defined in the cooling runs of DSC; those of **1** and **2** (260-270 °C) are higher than that of **3** (220 °C) probably because the longer π-conjugated structure, which prefers tight intermolecular π-π stacking. The thermal measurements suggest the possibility that the film morphology of **1-3** is improved by the thermal annealing.

Electrochemical and optical properties

The electrochemical and optical properties of **1-3** have been investigated by cyclic voltammetry (CV) and UV-vis absorption spectra as summarized in Table 1. As shown in Fig. 2, **1** and **2** exhibit clearly separated two reversible oxidation couples and one partly reversible reduction wave. In **3**, however, both the oxidation and reduction waves are quasi-reversible. According to the empirical formula: $E_{HOMO} = -e(E_{ox1}^{1/2} + 4.8)$ eV and $E_{LUMO} = -e(E_{red}^{1/2} + 4.8$ eV),[42] the HOMO levels of **1-3** are determined as shown in Table 1. The LUMO energies of **1-3** are almost the same. **1** and **2** have by about 0.6 V higher HOMO levels than **3** due to the electron donating character of the thiophene ring. The resulting high HOMO levels reduce the HOMO-LUMO gaps E_g in **1** and **2** (Table 1). These estimations are in basic agreement with the DFT calculations.

The UV-vis absorption spectra of solution and thin-film **1-3** are shown in Fig. 3. It is clear that both **1** and **2** have almost identical absorption profiles. In solutions of **1** and **2**, two absorption bands of 310 - 450 nm and 500 - 770 nm are observed. In contrast, **3** shows
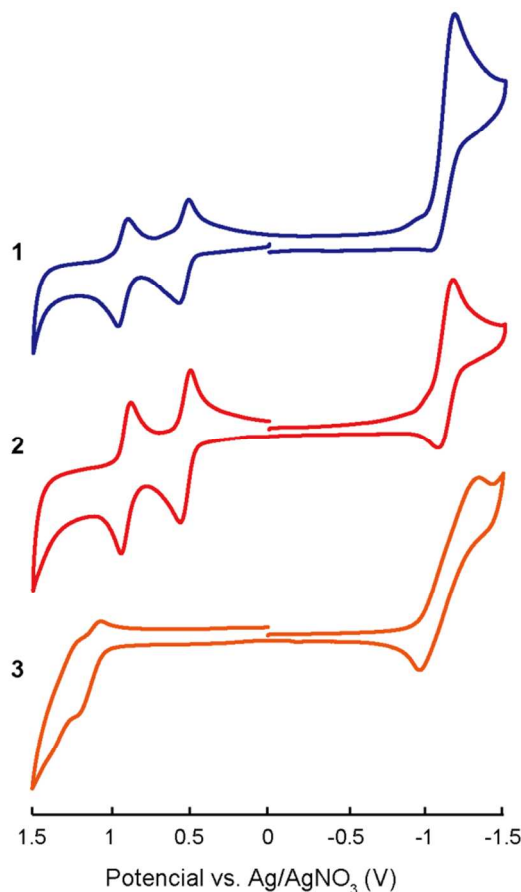
**Fig. 2** Cyclic voltammograms of **1-3** measured in 0.1 M Bu$_4$NPF$_6$ in CH$_2$Cl$_2$ at a scan rate of 100 mV^{-1}.

Table 1 Electrochemical and optical properties

Compound	$E_{ox1}^{1/2}$ (V)[a]	$E_{ox2}^{1/2}$ (V)[a]	$E_{red}^{1/2}$ (V)[a]	E_{HOMO} (eV)	E_{LUMO} (eV)	$E_{g, CV}$ (eV)	$\lambda_{abs, max}^{sol.}$ (nm)[b]	$\lambda_{abs, max}^{film}$ (nm)	$E_{g, op}$ (eV)[c]
1	0.54	0.93	-1.17	-5.06	-3.34	1.72	384, 649	397, 643	1.64
2	0.53	0.87	-1.17	-5.05	-3.34	1.71	361, 650	370, 645	1.64
3	1.14	1.29	-1.15	-5.66	-3.36	2.00	318, 441, 560	323, 449	1.86

[a]Versus Ag/AgNO$_3$ in CHCl$_3$ with 0.1 M n-Bu$_4$NPF$_6$, grassy carbon working electrode, scan rate 100 mVs^{-1} at room temperature, where Fc/Fc$^+$ is 0.28 V.[41]
[b]Measured in 10^{-5} M CHCl$_3$ solutions. [c]Estimated from solution absorption onset.

three absorption bands at 318 nm, 441 nm, and 560 nm. Compared with **3**, the long-wavelength absorption of **1** and **2** is obviously coming from the TII unit. In addition to an increase of the π-conjugation length originating from the flat molecules, this is associated with the push-pull character from the electron-rich thiophene to the electron-poor carbonyl group of the TII unit. In the thin films, the main absorption bands become broader and the absorption edge is red-shifted due to the shoulder appearing in the long-wavelength region. This indicates considerable intermolecular interaction and aggregation in the solid state. From the absorption edges of **1-3** in solution, the corresponding optical energy gaps are estimated to be1.64 eV for **1** and **2** whereas 1.86 eV for **3**, which are consistent with the electrochemical results (Table 1).
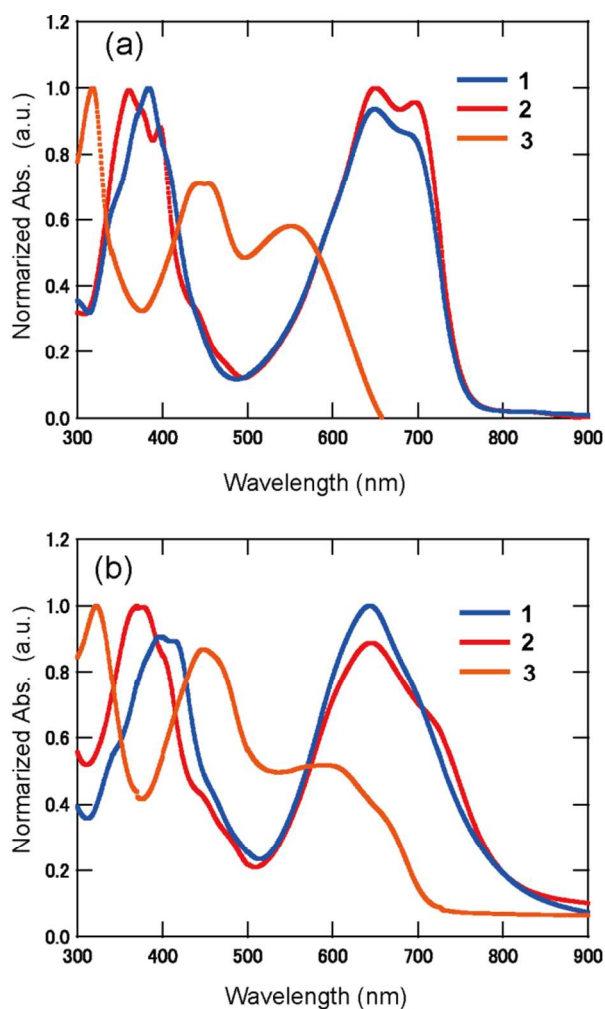
Fig. 3 Normalized UV/Vis absorption spectra of **1-3** for (a) CHCl$_3$ solutions (10^{-5} M), and (b) thin films spin-coated from CHCl$_3$ solutions.
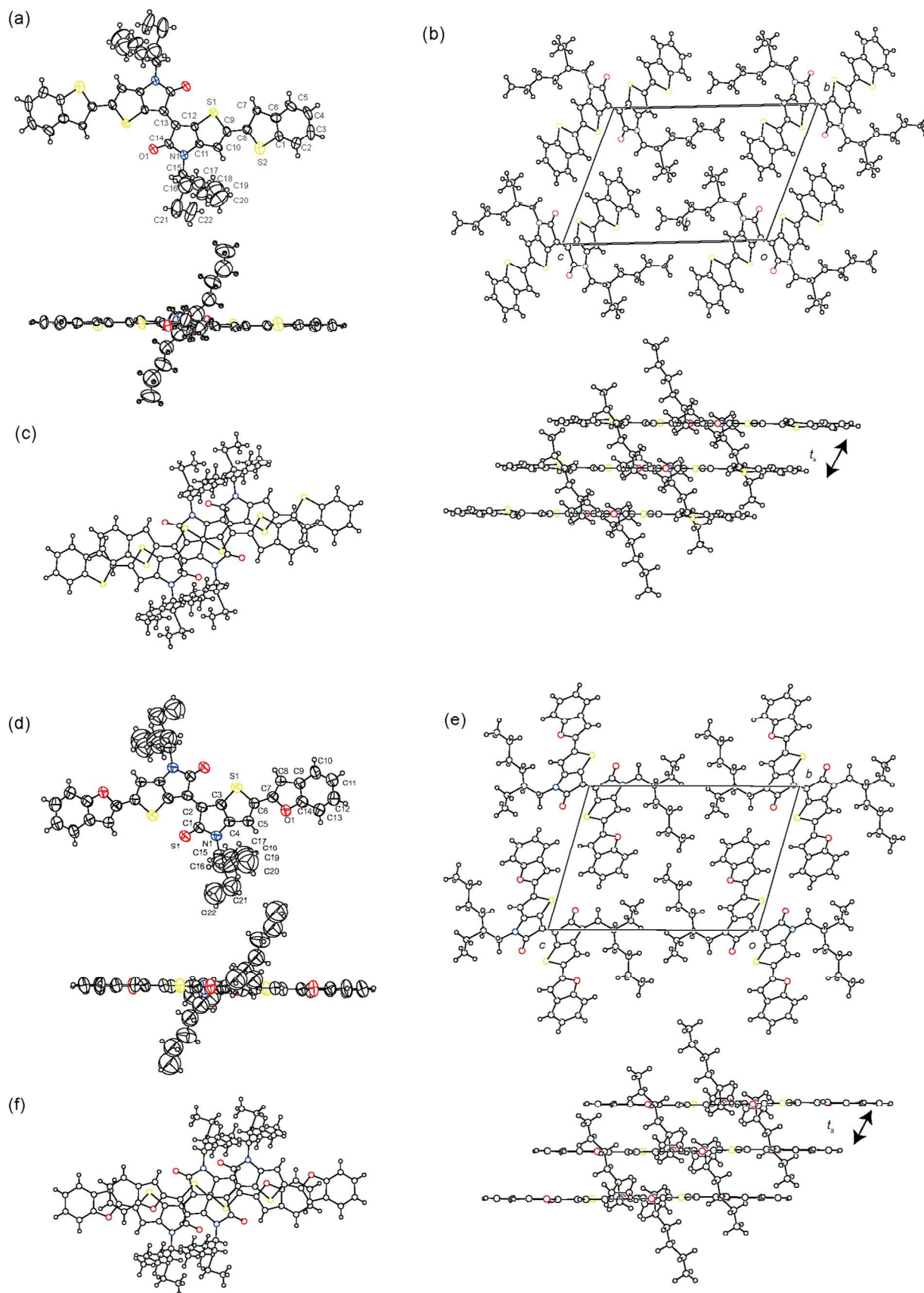
X-ray single-crystal structure analysis

X-ray structure analyses of **1** and **2** have been performed for single crystals grown by slow diffusion of hexane into CH$_2$Cl$_2$ solutions of **1** and **2**. The molecular and crystal structures are shown in Fig. 4, and the crystallographic data are listed in Table 2. Molecules **1** and **2** crystallize in the triclinic system with a space group $P(-1)$, in which a half molecule is crystallographically independent, and a unit cell contains one molecule located on an inversion center. The π-frameworks of **1** and **2** have planar geometry, agreeing with the DFT calculation, and the alkyl chains extend out of the molecular plane (Figs. 4(a) and 4(d)). As shown in Figs. 4(b) and 4(e), **1** and **2** make a slipped one-dimensional π-stacking, where an isoindigo part is basically located on another isoindigo part to form a "segregated" stack. In order to realize the co-facial segregated molecular packing, the planar π-framework is as important as the alkyl chains. The interplanar distance along the stack is 3.64 Å for **1** and 3.53 Å for **2**. The one-dimensional stacks are separated by the alkyl chains, leading to poor electronic coupling between the adjacent stacks. Transfer integrals estimated from the molecular orbital calculation also indicate highly one-dimensional transport; the HOMO transfer integrals along the stacks are $t_a = 43$ meV for **1** and $t_a = 130$ meV for **2**, and the LUMO transfer integrals are $t_a = 26$ meV for **1** and $t_a = 61$ meV for **2**, and other interstack transfers are negligible.[43] The smaller transfers in **1** are ascribable to the slightly larger interplanar distance of **1** and the resulting loose molecular packing within the stack, because the intermolecular overlap modes along the π-stacking in **1** and **2** are almost the same (Figs. 4(c) and 4(f)); the slip distances are 3.88 Å for **1** and 3.71 Å for **2** along the molecular long axis, and 0.38 Å for **1** and 0.87 Å for **2** along the molecular short axis.

Table 2 Crystallographic data of **1** and **2**

	1	**2**
Chemical formula	C$_{44}$H$_{46}$N$_2$O$_2$S$_4$	C$_{44}$H$_{46}$N$_2$O$_4$S$_2$
Crystal System	triclinic	triclinic
Formura weight	763.10	730.98
Shape	black needle	black needle
Space group	$P(-1)$	$P(-1)$
a / Å	5.21365(13)	5.1386(4)
b / Å	12.5465(3)	11.8573(9)
c / Å	16.7656(4)	16.4469(12)
α / °	110.3188(14)	105.425(5)
β / °	92.1751(15)	90.708(4)
γ / °	106.1216(14)	98.541(4)
V / Å^3	976.95(5)	953.88(13)
Z	1	1
D_{calc} / g cm^{-3}	1.297	1.272
Data / parameters	3510/215	3410/205
Goodness of fit on F_0^2	2.539	1.098
R_1[a] /Rw[b]	0.1344 /0.4030	0.1274/0.4022
Reflections used	3510($I > 2.00\sigma$)	3410($I > 2.00\sigma$)

[a] $R_1 = \sum \left| |F_0| - |F_c| \right| / \sum |F_0|$. [b] $R_w = \left[\sum w \left(|F_0| - |F_c| \right)^2 / \sum w F_0^2 \right]^{1/2}$

Fig. 4 (a) Molecular structure and (b) packing motif, and (c) overlap mode of **1**. (d) Molecular structure, (e) packing motif, and (f) overlap mode of **2**.

Table 3 Summary of FET characteristics[a]

| Compound	SAM	Mobility (cm^2 V^{-1} s^{-1})[a]	V_{th} (V)[a]	on/off ratio[a]
1	Bare	$\mu_h = 3.5 \times 10^{-3}$	-2.4	10^2
	HMDS	$\mu_h = 3.8 \times 10^{-3}$	-1.6	10^2
	OTMS	$\mu_h = 2.0 \times 10^{-2}$	16	10^2
	TTC[c]	$\mu_h = 2.2 \times 10^{-2}$	-5.2	10^3
		$\mu_e = 3.2 \times 10^{-2}$	-6.4	10^3
2	Bare	$\mu_h = 3.4 \times 10^{-3}$	-25	10^3
	HMDS	$\mu_h = 4.5 \times 10^{-3}$	-1.5	10^3
	OTMS	$\mu_h = 5.4 \times 10^{-3}$	1.0	10^4
	TTC[c]	$\mu_h = 5.8 \times 10^{-3}$	1.0	10^2
		$\mu_e = 1.0 \times 10^{-2}$	-5.1	10^3
3	Bare	$\mu_h = 2.7 \times 10^{-4}$	-55	10^2
	HMDS	$\mu_h = 5.5 \times 10^{-4}$	-40	10^3
	OTMS	$\mu_h = 5.4 \times 10^{-3}$	-9.9	10^4
	TTC[c]	$\mu_h = 3.5 \times 10^{-3}$	-8	10^4
		$\mu_e = 6.5 \times 10^{-3}$	11	10^4

[a]Average values for more than nine devices. All devices are measured under ambient conditions. The devices on TTC modified substrates showing ambipolar behavior are measured under vacuum.

Field-effect transistor performance

For comparing the FET properties, the FET devices with a bottom-gate and top-contact configuration were fabricated under the identical conditions; **1-3** were vapor deposited on Si/SiO$_2$ substrates modified with various self-assembled monolayer (SAM) treatments. The results are summarized in Table 3. Devices made of **1-3** exhibit basically p-channel transistor characteristics. Figure 5(a) shows p-channel output characteristics of **1** with the hole mobility of 0.020 cm^{2}V^{-1}s^{-1}. The TII-based transistors of **1** and **2** show that the hole mobilities ranging from 10^{-3} to 10^{-2} cm^{2}V^{-1}s^{-1} with the on/off current ratios of $10^2 – 10^4$. These values are one order of magnitude larger than those of the II-based **3**, and are comparable with those of the thienoisoindigo copolymers containing the D-A configuration. The p-channel threshold voltages of **1** and **2** are found to be positively shifted compared to **3** for the same SAM treatments (Bare, HMDS, and OTMS). This observation is related to the high HOMO levels of **1** and **2**. The HOMO and LUMO energy levels of **1** and **2** are located within the required region to exhibit ambipolar properties.[44] For the TTC modified devices, ambipolar behavior is observed similarly to the indigo device.[23, 24, 45] Figs. 5(b) and S2 demonstrate typical ambipolar behavior of **1** with the hole mobility of 0.022 cm^{2}V^{-1}s^{-1} and the electron mobility of 0.032 cm^{2}V^{-1}s^{-1}. The balanced motilities are associated with the appropriate HOMO and LUMO levels together with the delocalized FMO distribution.

Morphology of thin films

Figure 6 shows XRD patterns and AFM images of thin films of **1-3** for the TTC-modified substrates. Results for other SAM modified substrates are included in Figs S3 and S4. All XRD show sharp peaks corresponding to the d-spacings of 15-16 Å, which are slightly smaller than the c axies of the single-crystal X-ray structures. The single-crystal structures suggest that the molecules form a layered structure separated by the alkyl chains. Then the c axis is approximately perpendicular to the substrate, and the long axis of the π-skeleton is parallel to the substrate. The comparatively high mobility of **1** and **2** is associated with the stacking structure of the planar π-framework. The XRD indicates that **3** forms a similar
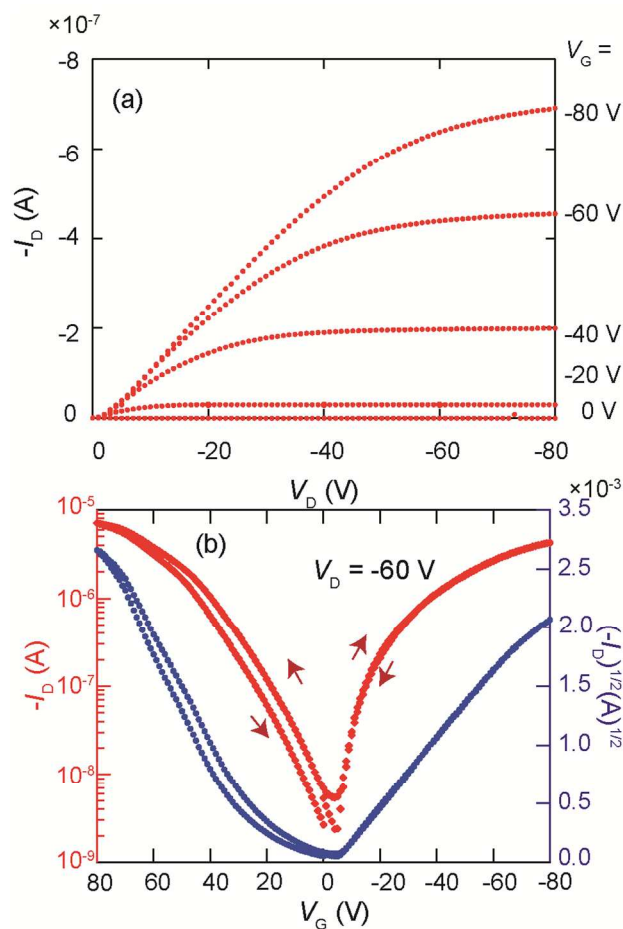
Fig. 5 (a) Transfer characteristics for TTC modified device and (b) p-channel output characteristics for OTMS modified device of **1**.

layered structure, though the core π-skeleton of **3** is expected to be nonplanar in view of the DFT calculation. The thin-film morphology of **1** and **2** largely depends on the SAM treatments, where the height and size of grains increase in the order of Bare < HMDS < OTMS< TTC (Figs. 6 and S3). The thin film of **3** consists of largely separated domains, which are probably related to the low mobility. It is noteworthy that the crystalline domains of the film of **1** fabricated on the TTC substrate is composed of characteristic fibrils highly ordered along the same orientation and small spherical grains (Fig. 6(d)). These small grains of **1** are also observed on HMDS substrate (Fig. S4(b). Therefore, the comparatively high mobility of **1** is probably due to the ordered fibril-like structures.

Solar cell performance

The bulkheterojunction OPVs of **1-3** were fabricated; the device structure was represented by ITO / PEDOT : PSS/ [molecules **1-3** : PC$_{71}$BM] / LiF / Al. The device performance was investigated under a AM 1.5 G illumination of 100 mW/cm^2. The active layer was spin-coated from the chloroform solution, where the concentration of the donor material was 10 mg/ml. The optimized donor and acceptor ratio was determined to be 3 : 2 by varying the acceptor percentage. The obtained films were annealed at different temperatures (as cast, 80 ℃, 110 ℃, and 150 ℃) to optimize the device performance. The device of **3** did not show noticeable response under the investigated conditions. The I-V curves and the external quantum efficiency
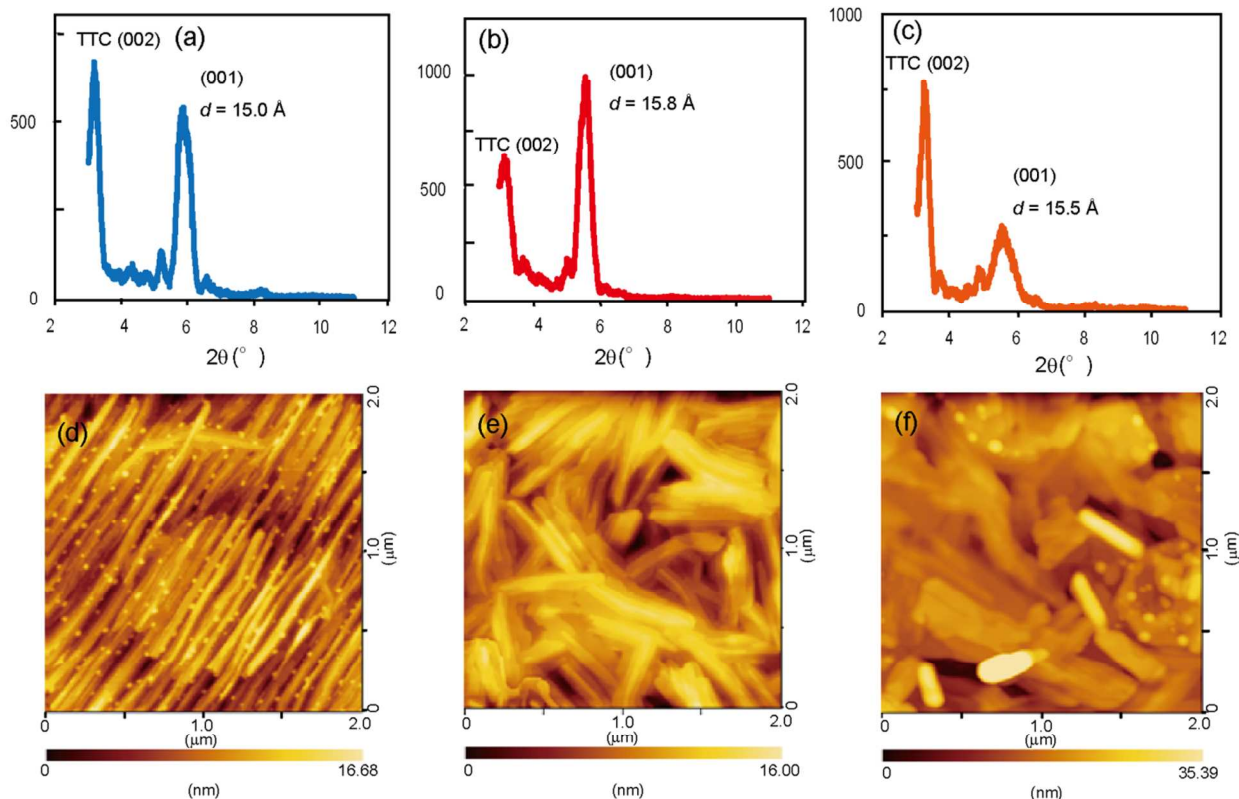
Fig. 6 XRD patterns of (a) **1**, (b) **2**, and (c) **3**. AFM images of thin films of (d) **1**, (e) **2**, and (f) **3**, thermally evaporated on TTC modified substrates.
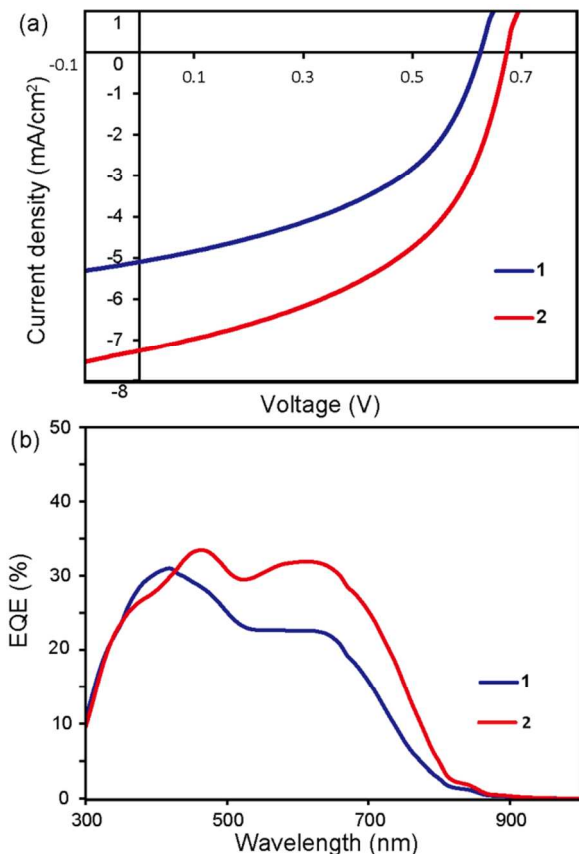

Fig. 7 (a) Photocurrent density-voltage (*J-V*) curves under illumination of AM 1.5G, 100 mWcm^{-2} and EQE curves of **1** and **2** under the optimized conditions.

(EQE) spectra of the OPV devices made of **1** and **2** are shown in Fig. 7. Table 4 summarizes the extracted photovoltaic parameters, including the short-circuit current density (J_{sc}), the open-circuit voltage (V_{oc}), the fill factor (*FF*), and the power conversion efficiency (PCE). These OPV devices show the best PCE of 1.5% for **1** and 2.4% for **2**. The V_{oc} of these devices is explained by the HOMO levels of **1** and **2** (-5.0 eV from Table 1) and LUMO level (-4.0 eV) of PC$_{71}$BM according to the equation, $V_{oc} = (1/e)(E_{HOMO, donor} - E_{LUMO, acceptor})$-0.3 V).[34 46-49] As shown in Fig. 7(b), devises of **1** and **2** exhibit a significantly broad photo-response curves ranging from 400 to 850 nm. The EQE curves contain two structures at 300-500 nm and 500-850 nm corresponding to the UV-vis absorption peaks of the films of **1** and **2** (Fig. 3(b)). The EQE of **2** is higher than that of **1** over the almost all wavelength, then higher J_{sc} values of **2** are obtained, and this is the reason that **2** shows better PCE than **1**. The morphology of the active layer is a key factor to determine the photovoltaic performance. Since the electronic structure of **1** and **2** are quite similar, the different response is expected to come from the different morphology of the blended thin films.

The blended films of **1-3** are investigated by AFM (Fig. 8) and XRD (Fig. S5) before and after the annealing. With increasing the annealing temperature, the domain size increases. The poorly connected grains of the blended films of **3** annealed at 80 °C, 110 °C, and 150 °C would be related to the absence of the solar cell performance. Comparing the blended films of **1** and **2**, larger grains of **1** are considered to be more preferable for the charge transport, and afford the improved J_{sc} values. With increasing the annealing temperature, **1** and **2** show maximum PCE at 110 °C (Table 4). When the temperature is further increased to 150

Table 4 Photovoltaic properties of the OPVs made of **1-3** and hole and electron motilities measured by the SCLC method.

Compound	Annealing	J_{SC} (mA/cm^2)	V_{OC} (V)	FF	PCE (%)	μ_h (cm^2/Vs)	μ_e (cm^2/Vs)
1	As-cast	2.18	0.65	0.29	0.4	4.0×10^{-7}	2.8×10^{-7}
	80	4.76	0.64	0.40	1.2	1.5×10^{-6}	2.1×10^{-6}
	110	5.16	0.64	0.46	1.5	2.7×10^{-6}	1.1×10^{-6}
	150	4.09	0.62	0.52	1.3	1.5×10^{-5}	2.3×10^{-5}
2	As-cast	4.68	0.70	0.36	1.1	2.1×10^{-6}	4.2×10^{-6}
	80	6.18	0.68	0.39	1.6	1.3×10^{-5}	3.6×10^{-5}
	110	7.26	0.67	0.49	2.4	1.8×10^{-5}	4.7×10^{-6}
	150	5.79	0.68	0.48	1.9	3.5×10^{-5}	1.2×10^{-4}
3	As-cast	N/A	-	-	-	1.9×10^{-9}	4.2×10^{-6}
	80	N/A	-	-	-	1.5×10^{-6}	5.5×10^{-6}
	110	N/A	-	-	-	8.3×10^{-7}	4.3×10^{-6}
	150	N/A	-	-	-	1.0×10^{-6}	4.3×10^{-6}
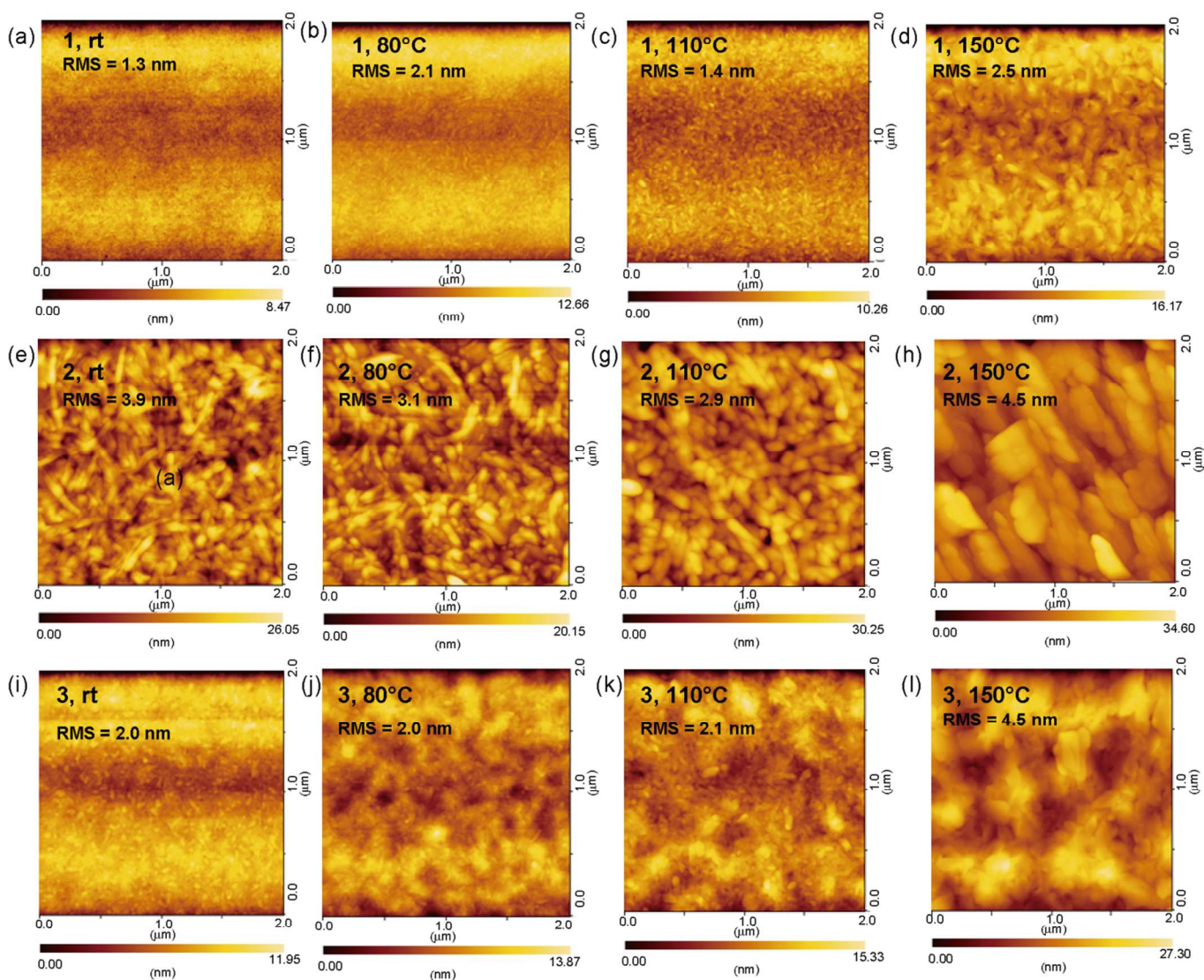
Fig. 8 AFM images of the bulkheterojunction active layers at increasing annealing temperature of (a)-(d) for **1** and (e)-(h) for **2**, and (i)-(l) for **3**.

ºC, the domain size becomes too large to the efficient charge separation, in agreement with the decreasing PCEs. In order to investigate the vertical carrier transport of the organic photovoltaic (OPV) devices, we have measured the hole- and electron-mobilities for the blended films of **1-3** using the space-charge limited current (SCLC) method. The SCLC curves are obtained using hole-only and

electron-only devices with the structures of ITO / PEDOT:PSS / molecules **1-3**: PC$_{71}$BM / Au for a hole device and Al / molecules **1-3**: PC$_{71}$BM / LiF / Al for an electron device, and the mobilities are estimated using the Mott-Gurney equation (Table 4).[50, 51] The measured SCLC hole motilities are in the order of 10^{-7} - 10^{-5} cm^{2}V^{-1}s^{-1} for **1**, 10^{-6} - 10^{-5}cm^{2}V^{-1}s^{-1} for **2**, and 10^{-9} - 10^{-6} cm^{2}V^{-1}s^{-1} for **3**, and electron motilities are in the order of 10^{-6} - 10^{-5} cm^{2}V^{-1}s^{-1} for **1**, 10^{-6} - 10^{-4}cm^{2}V^{-1}s^{-1} for **2**, and 10^{-6} cm^{2}V^{-1}s^{-1} for **3**. When compared under the identical annealing conditions, the low hole mobility of the films of **3** account for the absence of the OPV performance in **3**. It is noted that **2** shows higher hole mobilities than those of **1** under the same annealing conditions. These higher values are responsible for the improved device performance of **2**. The *d*-spacings of the XRD profiles in the blended films (Fig. S5) are almost the same as the evaporated pure **1-3** films as shown in Figs. 6 and S3. Molecules **1-3** show similar crystalline order even in the blended films. Among the XRD profiles, the blended films of **2** display a clearest diffraction peak (Fig. S5), to indicate that **2** forms a highly crystalline film contributing to the enhanced hole mobility observed in the SCLC measurement. The SCLC measurements demonstrate that the blended films with the hole mobility in the order of 10^{-7} cm^{2}V^{-1}s^{-1} show OPV characteristics, but those less than 10^{-7} cm^{2}V^{-1}s^{-1} do not show OPV characteristics. The estimated mobility suffers from a lot of microscopic factors such as the extent of interfacial traps, the molecular crystalline order, and the phase separation with the PC$_{71}$BM part. The comparatively low mobility limit for the OPV operation seems to be related to the balance to the electron mobility. As discussed from the viewpoint of the molecular planarity, the chemical modification of the central molecular framework drastically changes the performance of the FET and OPV devices by modifying the thin film morphology coming from the long-range molecular order. In addition to tuning the electronic structure, the design of molecular planarity is an important factor to improve the device performance.

Experimental

General

All the chemicals and solvents were of reagent grade unless otherwise indicated. All reactions were carried out under an argon atmosphere. The ^{1}H-NMR and ^{13}C-NMR spectra of the materials were recorded with a JEOL JNM-AL300 spectrometer (300 MHz) in CDCl$_3$ and tetramethylsilane was used as the internal standard. MS spectra were obtained with Shimadzu QP-5000 for EI-MS. MALDI-TOF mass spectrometry was performed using Shimadzu MALDI-AXIMA time of flight mass spectrometer. Microanalyses were performed at the Microanalysis Center, Tokyo Institute of Technology.

Molecular orbital calculation

Molecular orbital calculations were carried out using the Gaussian 09 program based on the B3LYP/6-31G*(d,p) .[39]

Material synthesis

Dibromothienoisoindigo **4** and dibromoisoindigo **5** were prepared according to the previous report.[33, 40]

Synthesis of compound 1

A mixture of compound **4** (0.49 g, 0.75 mmol), benzothienylboronic acid (0.33 g, 1.87 mmol) Pd(PPh$_3$)$_4$ (0.086 g, 0.075 mmol), aliquat336 (2 drops), and sodium carbonate (0.29 g, 2.76 mmol) in toluene (40 ml), ethanol (5 ml), and water (5 ml) was heated under

reflux for 24h and cooled. After quenching with water (50 ml), the aqueous layer was extracted with dichloromethane three times. The combined organic layer was washed with water and dried over anhydrous MgSO$_4$. After evaporation of the solvent, the crude product was purified by silica gel column chromatography using dichloromethane/hexane (2:1 v/v) as eluent, and recrystallization from toluene afforded 1 as a dark brown solid (0.29 g, 51%). Slow diffusion of hexane into a chloroform solution of 1 gave dark brown needles suitable for single-crystal X-ray analysis. M.p. = 290 °C (DSC). ^{1}H NMR (300 MHz, CDCl$_3$): δ 7.80 (d, *J* = 6.9 Hz, 2H), 7.75 (d, J = 5.7Hz, 2H), 7.63 (s, 2H), 7.37-7.33 (m, 4H), 6.96 (s, 2H), 3.72 (d, *J* = 7.8 Hz, 4H), 1.87-1.78 (m, 2H), 1.44-1.32 (m, 16H), 0.99-0.91 (m, 12H). MS (MALDI-TOF) m/z: 762.24 (M$^+$). Elemental analysis: Calcd for C$_{44}$H$_{46}$N$_2$O$_2$S$_4$: C, 69.25; H, 6.08; N, 3.67. Found: C, 69.11; H, 5.97; N, 3.61.

Synthesis of compound 2

Quantities were as follows: compound **4** (0.33 g, 0.50 mmol), benzofuranyllboronic acid (0.18 g, 1.11 mmol), Pd(PPh$_3$)$_4$ (0.058 g, 0.05 mmol), aliquat336 (2 drops), and sodium carbonate (0.20 g, 1.86 mmol). Purification by silica gel column chromatography and recrystallization gave a dark brown solid of **2** (0.22 g, 60%). Slow diffusion of hexane into a chloroform solution of **2** gave dark brown needles suitable for single-crystal X-ray analysis. M.p. = 292 °C (DSC). ^{1}H NMR (300 MHz, CDCl$_3$): δ 7.58 (d, *J* = 7.3 Hz, 4H), 7.49 (d, J = 7.7 Hz, 4H), 7.35-7.21 (m, 4H), 7.13 (s, 2H), 7.06 (s, 2H), 3.76 (d, *J* = 7.5 Hz, 4H), 1.93-1.87 (m, 2H), 1.53-1.25 (m, 16H), 0.99-0.91 (m, 12H). MS (MALDI-TOF) m/z: 730.29 (M$^+$). Elemental analysis: Calcd for C$_{44}$H$_{46}$N$_2$O$_4$S$_2$: C, 72.30; H, 6.34; N, 3.83; O, 8.75; S, 8.77. Found: C, 72.12; H, 6.27; N, 3.80; O, 8.45; S, 8.52.

Synthesis of compound 3

Quantities were as follows: compound **5** (1.29 g, 2.00 mmol), benzothienylboronic acid (0.71 g, 4.00 mmol), Pd(PPh$_3$)$_4$ (0.12 g, 0.20 mmol), aliquat336 (2 drops), and sodium carbonate (0.78 g, 7.40 mmol). Purification by silica gel column chromatography and recrystallization gave a dark brown solid of **2** (0.22 g, 60%). M.p. = 250 °C (DSC). ^{1}H NMR (300 MHz, CDCl$_3$): δ 9.22 (d, *J* = 9.0 Hz, 2H), 7.66 (d, J = 9.0 Hz, 2H), 7.50-7.35 (m, 8H), 7.10 (s, 2H), 3.76 (d, *J* = 5.2 Hz, 4H), 1.97-1.88 (m, 2H), 1.42-1.38 (m, 16H), 0.99-0.93 (m, 12H). MS (MALDI-TOF) m/z: 762.04 (M$^+$). Elemental analysis: Calcd for C$_{48}$H$_{50}$N$_2$O$_2$S$_2$: C, 76.73; H, 6.71; N, 3.73; O, 4.26; S, 8.54. Found: C, 76.73; H, 6.71; N, 3.73; O, 4.51; S, 8.29.

Thermal properties

Differential scanning calorimetric (DSC) measurements were performed with SII EXSTAR DSC-6100. Thermogravimetric analyses (TGA) were performed using SII EXSTA TG/DTA 7300. The heating rate was 5 °C / min for the DSC measurements and 10 °C / min for the TGA measurements in nitrogen. For the DSC measurements, the second heating-cooling cycles were analyzed.

Redox and optical properties

Cyclic voltammetry (CV) was performed with a ALS / CH Instruments Electrochemical analyzer Model 700C. The measurement was performed in a dichloromethane solution containing the present compound (0.2 mM) and tetra-*n*-butylammonium hexafluorophosphate (0.1 M) as a supporting electrolyte by the use of a glassy carbon working electrode, a

platinum counter electrode, and an Ag / AgNO₃ electrode as a reference electrode at a scan rate of 100 mV/s. UV-vis absorption spectra in a 10^{-5} M chloroform solution were recorded with a Jasco V-630 spectrometer. From the half-wave oxidation and reduction potentials $E_{ox}^{1/2}$ and $E_{red}^{1/2}$, the HOMO and LUMO levels were estimated by assuming the ferrocene/ferrocenium energy level to be -4.8 eV below the vacuum level.[42] The optical HOMO-LUMO energy gaps $E_{g, op}$ were estimated from the low-energy band edge of the absorption spectra.

X-ray single crystal structure analysis

The crystal structures were determined from single-crystal X-ray diffraction data. The measurements were made on a RIGAKU R-AXIS RAPID II imaging plate with Cu-Kα radiation from a rotation anode source with a confocal miltilayer X-ray mirror (RIGAKU VM-spider, λ = 1.54187 Å). The structures were solved by the direct method (SHELX-97).[52] The structures were refined by the full-matrix least-squares procedure by applying anisotropic temperature factors except for several atoms owing to the poor crystal quality. The positions of hydrogen atoms were calculated.

Transistor fabrication and thin-film characterization.

The OFET devices were fabricated on a heavily doped n⁺-Si wafer with a 300 nm thermally grown SiO_2 dielectric layer. After treatment with piranha solution for 15 min and washing by ultrasonicationor with ultrapure water for 10 min three times, the substrates were dried in an oven at 150 °C for 1h. The substrate were subjected to the SAM treatments. For hexamethyldisilazane (HMDS) treatment, the washed substrates were exposed in a HMDS vapor at 150 °C for 1 h. The substrates were washed three times with acetone for 20 min to remove excess HMDS on the substrate. For the octyltrimethoxysilane (OTMS) treatment, an OTMS solution (3 mM) in 1,1,2-trichloroethane (TCE) were spin-coated on the washed substrate, followed by exposure in an NH_3 vapar at room temperature for 24h. The substrate were rinsed with ultrapuire water and sonicated with toluene to remove excess OTMS on the substrate, and dried under vacuum. For the TTC treatment, TTC was thermally evaporated to form 20 nm TTC layer on the washed substrate. OFETs with top-contact source and drain (S/D) Au electrodes were fabricated. All organic semiconductors were thermally deposited under vacuum of ca. 1.0×10^{-4} Pa, where the resulting thickness was 50 nm. Au electrodes were thermally deposited under vacuum on the top of the active layer using a shadow mask with the channel length (L) of 50-200 μm and the width (W) of 1 mm. Characteristics of the OFET devices were measured at room temperature in air with a Keithley 4200 semiconductor parameter analyzer under the ambient conditions. For the detection of ambipolar performance, the measurement was carried out under vacuum. The field-effect mobility (μ) was calculated in the saturation region using an equation, $I_{DS} = \mu(WC_i/2L)(V_G-V_{th})^2$, where I_{DS} is the drain current, C_i is the capacitance of the SiO_2 dielectric layer, and V_G and V_{th} are the gate and threshold voltages, respectively. The capacitance including the TTC layer on an SiO_2 substrate were calculated to be 1.25×10^{-8} Fcm^{-2}.[53,54] Current on/off ratio (I_{on}/I_{off}) was determined from the minimum and the maximum of I_{DS}. X-ray diffraction (XRD) measurements were carried out on a Phillip X-PERT MPD-OEC with Cu Kα radiation (λ = 1.541 Å). Atomic force microscopic (AFM) images of the thin films on OFET and OPV were obtained by using a SII Nanonavi SPA-400 scanning probe microscope with SII SI-DF40 cantilever.

Solar cell fabrication.

All solar cells were fabricated using the same fabrication procedure as follows; the indium tin oxide (ITO)-coated glass substrate was thoroughly cleaned by ultrasonication in neutral and alkaline detergent, ultrapure water, acetone, and isopropyl alcohol. After complete drying, the ITO-coated glass was treated with UV-ozone. PEDOT:PSS (Clevios™ P AI4083, Heraeus) was spin-coated to a thickness of 30 nm, dried at 180 °C for 15 min in air and then transferred to an argon-filled glove box. A mixture of TII or II-based molecule and PC₇₁BM in chloroform were spin-coated on the top of PEDOT:PSS layer at 2000 rpm for 45 sec leading to a thickness typically 100 nm. The cells were then thermally annealed on a hotplate at 80, 110, and 150 °C for 15 min. Subsequently, the electron transport layer (LiF, 0.7 nm) and the metal electrode (Al, 130 nm) were deposited by thermal evaporation under high vacuum condition (< 10^{-6} Torr). The active area of the cell is 4 mm². The current density-voltage (J-V) characteristics of the cell were measures using a Keithkey 2400 source measure unit. The solar cell performance was measured employing an air mass 1.5 global (AM1.5G) solar simulator (OTENTO-SUN III, Bunkoh-Keiki) with as irradiation intensity of 100 mWcm⁻². The illumination intensity was calibrated by a standard Si photodiode detector with KG-5 filter, and no additional mask was used under the illumination. The external quantum (EQE) spectra were measured using a MTE-1500 solar cell measurement system (Bunkoh-Keiki) including a Xe source, a monochrometer, an optical chopper and a lock-in amplifier, and a standard Si photodiode with KG-5 filter for monochromatic power-density calibration.

Hole and electron mobility measurement by the SCLC method.

To determine hole and electron mobilities, two types of devices, which were composed of ITO / PEDOT:PSS (30 nm) / molecules **1-3**: PC₇₁BM (100 nm) / Au and Al / molecules **1-3**: PC₇₁BM (100 nm) / LiF (7nm) / Al for the hole and electron mobility measurements, respectively, were fabricated. The mobility was determined by fitting the dark current to the space-charge-limited currents (SCLC) model described by the equation:[50,51]

$$J = (9/8) \, \varepsilon_0 \varepsilon_r \mu (V^2/L^3) \qquad (1)$$

where J is the current density, ε_r is the relative permittivity and assumed as approximately 3.0, ε_0 is the permittivity of free space, μ is the mobility, V is the effective voltage, and L is the thickness of the active layer. The mobility was calculated from the slope of the $J^{1/2}$ vs. V curves.

Conclusions

In summary, we have designed three organic semiconductors **1-3** composed of the central TII or II unit end-capped with benzothiophene or benzofuran units. The DFT calculation as well as the redox and optical measurements show that the TII-based **1** and **2** have an almost planar structure and a higher HOMO level with a small energy gap compared with the II-based **3**. These structural and electronic features are characteristic of the TII unit. From the single-crystal structure analyses of **1** and **2**, the π-frameworks of the TII-based **1** and **2** show high planarity as predicted by the DFT calculation, and form slipped one-dimensional stacks. The OFETs of **1-3** show typical p-channel properties. Charge-carrier motilities of **1** and **2** are one order of magnitude higher than that of **3**. Notably, the OFETs of **1** and **2** on TTC-modified substrates exhibit well balanced ambipolar performance resulting from the delocalization of the FMOs. The OPVs of **1** and **2** show photovoltaic performances with PCE up to 2.4% for **2** and 1.5%

for **1**, whereas the device of **3** does not work. The planar structure of the TII unit obviously changes the molecular packing and the thin-film morphology, and consequently improves the OFET and OPV properties. The present study provides a better understanding of structure-property relationship for the development of small-molecule organic semiconductors.

Acknowledgements

Notes and references

a Department of Organic and Polymeric Materials, Tokyo Institute of Technmology, O-okayama 2-12-1, Meguro-ku, Tokyo 152-8552

b ACT-C, JST, Honcho, Kawaguchu, 332-0012, Japan

† Electronic supporting information (ESI) available: CCDC 1024050–1024051 contain the supplementary crystallographic information of **1** and **2**. Additional information of thermal properties, AFM, and XRD measurements.

1. A. R. Murphy, J. M. J. Frechet. *Chem. Rev.* **2007**, *107*, 1066-1096.

2. A. Facchetti, *Mater. Today* **2007**, *10*, 28-37.

3. J. M. Anthony, A. Facchetti, M. Heeny, S. R. Marder, X. W. Zhan, *Adv. Mater.* **2010**, 22, 3876-3892.

4. J. Zaumseil, H. Sirringhaus, *Chem. Rev.* **2007**, 107, 1296-1323.

5. M. Bernius, M. Inbasekaran, E. Woo, W. S. Wu, L. Wujkowski, *Thin Solid Films* **2000**, *363*, 55-57.

6. R. H. Friend, R. W. Gymer, A. B. Holmes, J. H. Burroughes, R. N. Marks, C. Taliani, D. D. C. Bradley, D. A. D. Santos, J. L. Brédas, M. Lögdlund, *Nature,* 1999, **397**, 121-128.

7. Molecular OPVs: A. W. Hains, Z. Liang, M. A. Woodhouse, B. A. Gregg, *Chem. Rev.* 2010, **110**, 6689-6735.

8. Polymeric OPVs: Y. J. Cheng, S. H. Yang, C. S. Hsu, *Chem. Rev.* 2009, **109**, 5868-5923.

9. J. Zhou, Y. Zuo, X. Wan, G. Long, Q. Zhang, W. Ni, Y. Liu, Z. Li, G. He, C. Li, B. Kan, M. Li, Y. Chen, *J. Am. Chem. Soc.* 2013, **135**, 8484-8487.

10. Z. He, C. Zhong, X. Huang, W. -Y. Wong, H. Wu, L. Chen, S. Su, Y. Cao, *Adv. Mater*, **2011**, 23, 4636-4643.

11. J. Mei, Y. Diao, A. L. Appleton, L. Fang, Z. Bao. *J. Am. Chem. Soc.* **2013**, 135, 6724-6746.

12. S. Holliday, J. E. Donaghey, I. MuCulloch. *Chem. Mater.* **2014**, 26, 647-663.

13. A. Mishra, P. Bäuerle, *Angew. Chem. Int. Ed*., **2012**, 51, 2020-2067.

14. J. Zhou, Y. Zuo, X. Wan, G. long, Q. Zhang, W. Ni, Y. Liu, Z. Li, G. He, C. Li, B. Kan, M. Li, Y. Chen. *J. Am. Chem. Soc.* 2013, 135, 8484-8487.

15. X. Zhan, A. Facchetti, S. Barlow, T. J. Marks, M. A. Ratner, M. R. Wasielewski, S. R. Marder. *Adv. Mater*, **2011**, 23, 268-284.

16. Z. H. Chen, Y. Zheng, H. Yan, A. Faccetti. *J Am. Chem. Soc*., **2009**, 131, 8-9.

17. K. –H. Ong, S. –L, Lim, H. –S. Tan, H. –K. Wong, J. Li, Z. Ma, L. C. H. Moh, S. –H. Lim, J. C. De Mello, Z. –K. Chen, *Adv. Mater.*, **2011**, 23, 1409-1413.

18. J. Fan, J. D. Yuen, W. Cui, J. Seifter, A. R. Mohebbi, M. Wang, H. Zhou, A. J. Heeger, F. Wudl. *Adv. Mater*., **2012**, 24, 6164-6168.

19. J. D. Yuen, J. Fan, J. Seifter, B. Lim, R. Hufschmid, A. J. Heeger, F. Wudl. *J. Am. Chem. Soc.* **2011**, 133, 20799-20807.

20. J. Lee, A. R. Han, H. Yu, T. J. Shin, C. Yang, J. H. Oh. *J. Am. Chem. Soc*., **2013**, 135, 9540-9547.

21. I. Kang, H. –J. Yun, D. S. Chung, S. –K. Kwon, Y. –H. Kim. *J. Am. Chem. Soc.* **2013**, 14896-14899.

22. J. Li, Y. Zhao. H. S. Tan. Y. Guo, C. –A. Di, G. Yu, Y. Liu, M. Lin, S. H. Lim, Y. Zhou, H. Su, B. S. Ong. *Sci, Rep*. **2012**, 2, 754. Doi: 10.1038 / srep00754.

23. M. Irimia-Vlada, E.D. Glowacki, P. A. Troshin, G. Schwabegger, L. Leonat, D. K. Susarova, O. Krystal, M. Ullah, Y. Kanbur, M. A. Bodea, V. F. Razumov, H. Sitter, S. Bauer, N. S. Sariciftci. *Adv. Mater.* **2012**, 24, 375-380.

24. O. Pitayatanakul, T. Higashino, T. Tanaka, H. Kojima, M. Ashizawa, T. Kawamoto, H. Matsumoto, K. Ishikawa, and T. Mori, *J. Mater. Chem*. C, **2014**, doi: 10.1039/C4TC01563K.

25. E. D. Glowacki, G. Voss, N. S. Sariciftci. *Adv. Mater*. **2013**, 25, 6783-6799.

26. R. Stalder, J. Mei, K. R. Graham, L. A. Estrada, J. R. Reynolds. *Chem. Mater.*, **2014**, 26, 664-678.

27. J. Mei, D. H. Kim, A. L. Ayzner, M. F. Toney, Z. Bao, *J. Am. Chem.Soc.*, **2011**, 133, 20130-20133.

28. T. Lei, Y. Cao, X. Zhou, Y. Peng, J. Bian, J. Pei. *Chem. Mater.*, **2012**, 24, 1762-1770.

29. T. Lei, Y. Cao, Y. Fan, C. –J. Liu, S. –C. Yuan, J. Pei. *J. Am.Chem. Soc.*, **2011**, 133, 6099-6101.

30. G. W. P. Van Pruissen, F. Gholamrezaie, M. M. Wienk, R. A. J. Janssen. *J. Mater. Chem.* **2012**, 22, 20387-20393.

31. Y. Koizumi, M. Ide, A. Saeki, C. Vijayakumar, B. Balan, M. Kawamoto, S. Seki. *Polym. Chem.*, **2013**, 4, 484-494.

32. M. S. Chen, J. R. Niskala, D. A. Unruh, C. K. Chu, O. P. Lee, J. M. Fréchet. *Chem. Mater.* **2013**, 25, 4088-4096.

33. R. S. Ashraf, A. J. Kronemeijer, D. I. James, H. Sirringhaus, I. McCulloch. *Chem. Commun*., **2012**, 48, 3939-3941.

34. B. Walker, A. B. Tamayo, X. –D. Dang, P. Z. Jung, H. Seo, A. Garcia, M. Tantiwiwat, T. –Q. Nguyen. *Adv. Funct. Mater.*, **2009**, 19, 3063-3069.

35. Y. Zhang, X. –D. Dang, C. kim, T. –Q. Nguyen. *Adv. Energy Mater*., **2011**, 1, 610-617.

36. J. Liu, B. Walker. A. Tamayo, Y. Zhang, T. –Q. Nguyen. *Adv. Funct. Mater*., **2013**, 23, 47-56.

37. J. Liu, Y. Zhang, H. Phan, A. Sharenko, P. Moonsin, B. Walker, V. Promarak, T. –Q. Nguyen. *Adv. Mater.*, **2013**, 25, 3645-3650.

38. T. B. Henson, G. C. Welch, T. van der Poll, G. C. Bazan. *J. Am. Chem. Soc*., **2012**, 135, 3766-3779.

39. The molecular orbital calculation was carried out using the Gaussian 09, Revision B.01, Frisch, M. J.; Trucks, G. W.; Schlegel, H. B.; Scuseria, G. E.; Robb, M. A.; Cheeseman, J. R.; Scalmani, G.; Barone, V.; Mennucci, B.; Petersson, G. A.; Nakatsuji, H.; Caricato, M.; Li, X.; Hratchian, H. P.; Izmaylov, A. F.; Bloino, J.; Zheng, G.; Sonnenberg, J. L.; Hada, M.; Ehara, M.; Toyota, K.; Fukuda, R.;

Hasegawa, J.; Ishida, M.; Nakajima, T.; Honda, Y.; Kitao, O.; Nakai, H.; Vreven, T.; Montgomery, Jr., J. A.; Peralta, J. E.; Ogliaro, F.; Bearpark, M.; Heyd, J. J.; Brothers, E.; Kudin, K. N.; Staroverov, V. N.; Kobayashi, R.; Normand, J.; Raghavachari, K.; Rendell, A.; Burant, J. C.; Iyengar, S. S.; Tomasi, J.; Cossi, M.; Rega, N.; Millam, N. J.; Klene, M.; Knox, J. E.; Cross, J. B.; Bakken, V.; Adamo, C.; Jaramillo, J.; Gomperts, R.; Stratmann, R. E.; Yazyev, O.; Austin, A. J.; Cammi, R.; Pomelli, C.; Ochterski, J. W.; Martin, R. L.; Morokuma, K.; Zakrzewski, V. G.; Voth, G. A.; Salvador, P.; Dannenberg, J. J.; Dapprich, S.; Daniels, A. D.; Farkas, Ö.; Foresman, J. B.; Ortiz, J. V.; Cioslowski, J.; Fox, D. J. Gaussian, Inc., Wallingford CT, 2009.

40. J. Mei, K. R. Graham, R. Stalder, J. R. Reynolds. *Org. Lett.*, **2010**, 12, 660-663.

41. N. Miyaura, K. Yamada, A. Suzuki. *Tetrahedron Lett.* **1979**, 20, 3437-3440.

42. J. Pommerehne, H. Vestweber, W. Guss, R. F. Mark, H. Bässles, M. Porsch, J. Daub. *Adv. Mater.*, **1995**, 7, 551-554.

43. T. Mori, A. Kobayashi, Y. Sasaki, H. Kobayashi, G. Saito,H. Inokuchi. *Bull. Chem. Soc. Jpn.* **1984**, 57, 627-633.

44. M. L. Tang, A. D. Reichardt, P. Wei, Z. Bao. *J. Am. Chem. Soc.*, **2009**, 131, 5264-5273.

45. For the detection of ambipolar performance, especially n-channel performance, the measurement was carried out under vacuum.

46. M. C. Scharber, D. Muhlbacher, M. Koppe, P. Denk, C. Waldauf, A. J. Heeger, C. J. Brabec, *Adv. Mate*r. **2006**, 18, 789-794.

47. M. A. Loi, S. Toffanin, M. muccini, M. Forster, U. Scherf, M. Scharber, *Adv. Funct. Mater.*, **2007**, 17, 2111-2116.

48. C. Deibel, T. Strobel, V. Dyakonov, *Adv. Mater.*, **2010**, 22, 4097-4111.

49. K. Vandewal, A. Gadisa, W. D. Oosterbaan, S. Bertho, F. Banishoeib, I. V. Severen, L. Lutsen, T. J. Cleij, C. Vanderzande, J. V. Manca, *Adv. Funct. Mater.*, **2008**, 18, 2064-2070.

50. P. W. M. Blom, M. J. M. de Jong, M. G. van Munster. *Phys. Rev. B: Condens, Matter Mater. Phys.*, **1997**, 55, R656-R659.

51. Z. Li, Q. Dong, Y. Li, B. Xu, M. Deng, J. Pei, J. Zhang, F. Chen, S. Wen, Y. Gao, W. Tian. *J. Mater. Chem.*, **2011**, 21, 2159-2168.

52. Sheldrick, G. M.; *Acta cryst.* **2008**, *A64*, 112-122.

53. M. Kraus, S. Richler, A. Opitz, W. Brutting, S. Haas, T. Hasegawa, A. Hinderhofer, F. Schreiber, *J. Appl. Phys.* **2010**, 107, 094503-1-094503-6.

54. K. J. Baeg, Y. Y. Noh, J. Ghim, B. Lim, and D.Y.Kim. *Adv. Funct. Mater.* **2008**, *18*, 3678-3685.

Table of contents

Structure-property relationship

23.9° 11.3° 23.9°

$\mu_h = 2.2 \times 10^{-2}$ cm²/Vs
$\mu_e = 3.2 \times 10^{-2}$ cm²/Vs
$PCE = 1.5\%$

$\mu_h = 5.8 \times 10^{-3}$ cm²/Vs
$\mu_e = 1.0 \times 10^{-2}$ cm²/Vs
$PCE = 2.6\%$

$\mu_h = 3.5 \times 10^{-3}$ cm²/Vs
$\mu_e = 6.5 \times 10^{-3}$ cm²/Vs